International Symposium
On Turbulence and Shear Flow
Phenomena (TSFP-9)
June 30 - July 3, 2015 *Melbourne, Australia*

LARGE-SCALE STRUCTURES IN SWIRLING JETS WITH BUBBLE- AND SPIRAL-TYPE VORTEX BREAKDOWN

Vladimir M. Dulin[1,2]*, Maxim V. Alekseenko[1,2], Artur V. Bilsky[1,2], Mikhail P. Tokarev[1,2], Dmitriy M. Markovich[1,2], Kemal Hanjalić[2,3]

1: Kutateladze Institute of Thermophysics,
1, Lavrentyev Avenue, Novosibirsk, 630090, Russia

2: Department of Science and Research
Novosibirsk State University
2, Pirogova Street, Novosibirsk, 630090, Russia

3: Chemical Engineering Department
Delft University of Technology
Julianalaan 136, 2628 BL Delft, The Netherlands
* vmd@itp.nsc.ru

ABSTRACT

We report on a parallel study of the dynamics of large-scale vortical structures in low- and high-swirl turbulent jets by means of the time-resolved tomographic PIV technique. The high-swirl jet is featured by a bubble-type vortex breakdown with a central recirculation zone. In the low-swirl flow the mean axial velocity remains positive although with a local velocity defect immediately downstream from the nozzle exit, followed by spiralling vortex system and its eventual breakdown. Precessing vortex core is detected in both flows, but the POD analysis showed that the one originating in the bubble-type vortex-breakdown is much more energetic and easier to detect.

FOCUS OF THE STUDY

Because of their rich physics and versatile application (enhancing mixing, phase separation, flame stabilization), swirling flows have been the subject of extensive investigations. Various structures have been identified: precessing vortex core (PVC), multiple spiralling vortices, vortex breakdown (VB) and formation of the central recirculation zone (RZ). Experimental studies using flow visualisation, pointwise velocimetry, planar velocimetry via light sheet illumination, and data processing with various decomposition techniques, all complemented with numerical simulations, have brought much insight into the flow structures and their dynamics, but some issues still await full clarification. For example, Brücker (1993) found that at low Re numbers (~150) the spiral and bubble vortex breakdowns manifest similar flow features. For the latter, a bubble-type recirculation zone (RZ) can be clearly detected, while in the former case, the swirling core takes form of a spiralling helix caused by a faster retardation of the axial velocity after expansion. At high Re the bubble-type VB is usually accompanied by a strong precession, but it is not clear if the PVC appears in the turbulent spiral-type VB regime at similar Re numbers.

The recirculation zone in high-swirl jets and velocity-defect in low-swirl jets are known to provide stabilisation of flames, but the second case is preferable for NOx reduction (e.g., see Johnson et al., 2005). However, the importance of the PVC for flame stabilisation is still a debated issue. Recently, Markovich et al. (2014) argued that PVC is present both in low- and high-swirl jets and flames. Admittedly, this contradicts some earlier findings that PVC appears only at high swirls. The latter claim is based on the fact that PVC is often detected by conditional sampling in high-swirl flows because it is congruent with global flow oscillations, whereas in low-swirl flows (rotating spiralling helix) PVC is usually not extracted by conditional sampling because it is not sufficiently energetic and not associated with a specific, but rather with a range of frequencies.

The present paper complements the planar high-speed PIV measurements reported in Markovich et al. (2014) with new results for the 3D velocity field obtained by a high-speed tomographic PIV system. The results provide a new insight into the dynamics of large-scale vortex structures including PVC in turbulent low- and high-swirl jets, featured respectively by spiral- and the bubble- type vortex breakdown.

EXPERIMENTAL SETUP AND DATA PROCESSING

The swirling jet flow was organized in a closed hydrodynamic circuit, which included a water tank, pump, flow meter, and test section. The flowrate was controlled via feedback from the flow meter to the pump. The origin of a Cartesian coordinate system (x, y, z) is located at the centre of the nozzle exit. The axis y coincides with the jet axis. The coordinate z is directed towards the PIV cameras (see Figure 1).

The rectangular test section (200×600×200 mm^3) was made of Plexiglas. A contraction nozzle with changeable vane swirlers inside produced the swirling jet flows.

Details on the nozzle can be found in Alekseenko et al. (2008). Using two swirlers with different inclination angle of the blades, the considered swirl rate S defined as (1) (Gupta et al. 1998) was 0.41 and 1.0.

$$S = \frac{2}{3}\left(\frac{1-(d_1/d_2)^3}{1-(d_1/d_2)^2}\right)\tan(\psi). \qquad (1)$$

Here, d_1 = 7 mm is the diameter of the centrebody supporting the blades, d_2 = 27 mm is the external diameter of the swirler, and ψ is the blade inclination angle. It is noted that equation (1) assumes uniform velocity profile between the blades with velocity direction parallel to the blades.

The swirler was mounted inside the nozzle as demonstrated in Figure 2a. The nozzle exit diameter d was 15 mm. The Reynolds number, defined as Re = $U_b d/\nu$ (U_b is the bulk flow velocity; ν is the water kinematic viscosity) was set to 8 900 (as in the previous study by Alekseenko et al., 2008).

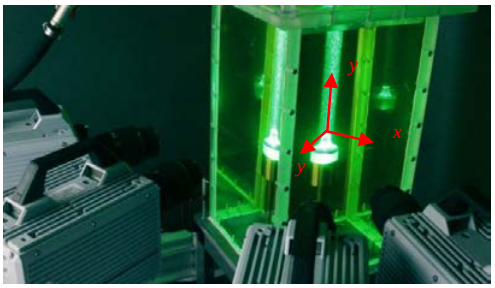

Figure 1. Photo of the experimental setup

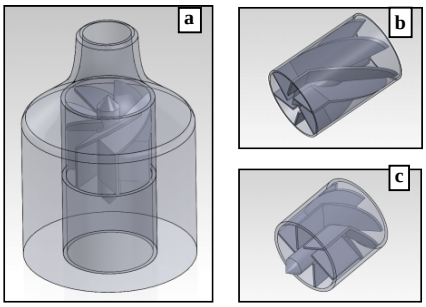

Figure 2. (a) Schematics of swirler arrangement in the nozzle, and images of the swirlers with (b) 30° and (c) 55° angles of blade inclination

For the PIV measurements the flow was seeded with 50 μm polyamide particles. The measurement volume of 2.5d×4d×2.5d was recorded by four high speed CMOS cameras (Photron FASTCAM SA5) with resolution of 1024×1024. The cameras were equipped with SIGMA AF 105 mm f/2.8 EX DG MACRO lenses. The measurement volume was illuminated by a high-repetition pulsed Nd:YAG laser (Photonix DM100-532) with the average power of 100 Watts. The cameras and laser were synchronized by BNC 575 device from Berkeley Nucleonics. The acquisition frequency was 2 kHz

The in-house "ActualFlow" software was used to measure and process the acquired data. The cameras were calibrated by capturing images of a plane target (150×150 mm) moved trough the measurement volume by a microscrew traverse. A self-calibration procedure (similar to that of Wieneke, 2008) was used prior to the tomographic reconstruction of the 3D images. The final average disparity was below 0.07 pixels and the corrected disparity was up to 10 pixels.

The size of the reconstructed 3D images was 643×571×643 voxels. The tomographic reconstruction was carried out by an advanced two-frame technique MLOS+15 SMART + 3× (MTE + 15 SMART) (Atkinson and Soria et al., 2009; Novara et al., 2010). Particles shift was evaluated by using an iterative multi-grid algorithm with continuous volume shift and deformation. The grid-overlapping factor was set to 75%. The final size of the correlation domain for the calculation of a single velocity vector was 2.8×2.8×2.8 mm^3 (40×40×40 voxels). Two thousand velocity fields were obtained for each flow case.

SOME RESULTS AND DISCUSSION

The high-swirl case, S = 1.0, is featured by a pronounced bubble-type breakdown of the swirling jet, preceded by a two-shear-layers. The inner shear layer was formed between the annular jet and the bubble-type central RZ, and the outer shear layer between the jet and the surrounding water. Figure 3 shows the spatial distributions of the mean velocity and turbulent kinetic energy (TKE), measured in the central plane by 2D (stereoscopic) PIV system in the previous work by Alekseenko et al. (2008). The solid line bounds the central recirculation zone with negative axial velocity.

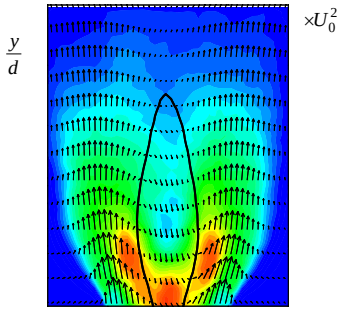

Figure 3. Mean velocity field and TKE distribution for a high-swirl jet (S = 1.0, Re = 8 900, 2D PIV)

For the low swirl, S = 0.41, the mean velocity field and TKE distribution are shown in Figure 4. The flow retards around the axis due to the jet expansion and swirl-induced pressure gradient, but the mean axial velocity remains positive. Most intensive velocity fluctuations are observed around the jet axis, where the axial velocity is decreasing.

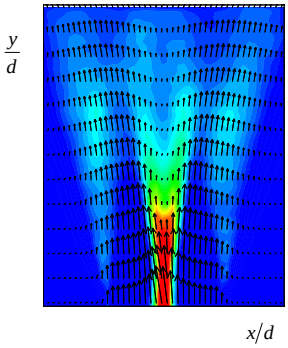

Figure 4. Mean velocity field and TKE distribution for a low-swirl jet (S = 0.41, Re = 8 900, 2D PIV)

Figures 5 and 6 show the mean velocity data measured by 3D PIV for the high- and low-swirl jets, respectively. The magnitude of the axial mean velocity, visualized in two planes perpendicular to the jet axis, confirms that the 3D technique resolves the round shape of the jets. Direct comparison of 3D and 2D velocity measurements for the high-swirl jet was reported previously by Alekseenko et al (2014) for low-speed 3D PIV measurements. It is noted here, that a strong spatial smoothing effect on 3D PIV data is detected for the high-swirl jet in the vicinity of the nozzle.

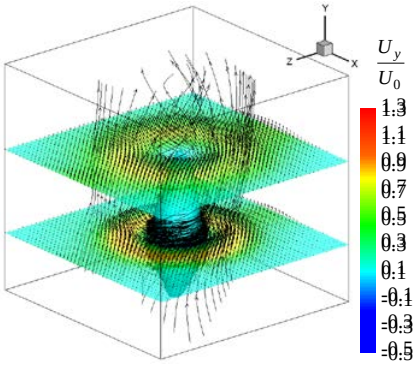

Figure 5. Mean velocity field for a high-swirl jet (S = 1.0, Re = 8 900, 3D PIV)

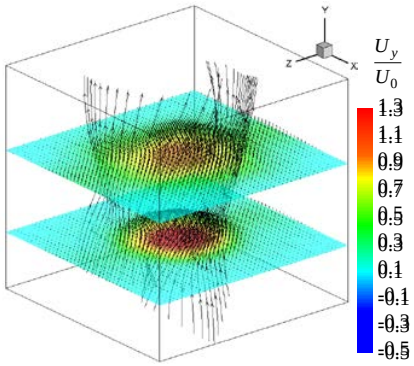

Figure 6. Mean velocity field for a low-swirl jet (S = 0.41, Re = 8 900, 3D PIV)

The three-dimensional plots of the mean streamlines in Figures 5 and 6 clearly show that the residence time (relevant for two phase flows and combustion) in the central reverse flow in the high-swirl jet should be greater than in the low-swirl case with no reverse flow. An instantaneous snapshots in Figure 7a with the bound of the reverse flow $U_y = 0$ denoted by a non-transparent surface shows a bubble of a similar size as in Figures 3 and 5, but it is asymmetric. This confirms that the shape of the reverse flow region is associated with asymmetry (helical disturbance is highlighted by dash lines) of the annular jet (visualized by the partially transparent surfaces of $U_y = 0.25U_0$).

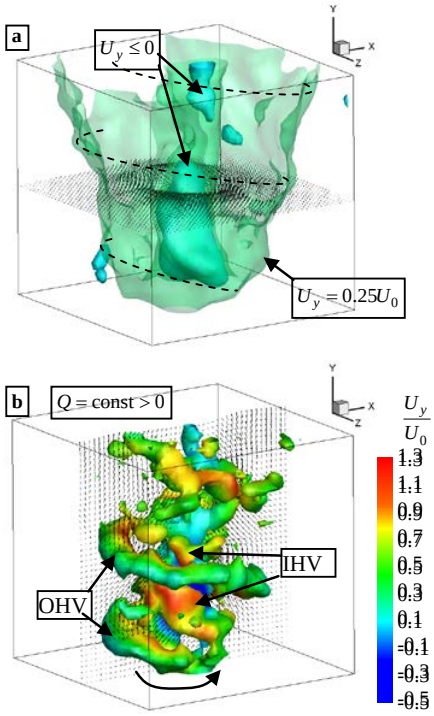

Figure 7. The instantaneous velocity data for a high-swirl jet (S = 1.0, Re = 8 900, 3D PIV)

Figure 7b reveals that the inner and outer mixing layers of the high-swirl jet are associated with large-scale spiraling vortex structures, here educted by iso-surfaces of positive Q-criterion (Hunt et al., 1988) and colored by the local values of the axial velocity component. This helps to distinguish the outer helical vortex (marked by OHV) in the outer mixing layer from the inner helical vortex (IHV) in the inner layer. For the OHV the surface is associated with positive U_y on the inner side (close the jet axis) of the spiraling surface, and vise versa for the IHV.

The outer helix is winding in the direction opposite to that of the swirl (the direction of the jet angular velocity). In contrast the direction of the outer helix rotation (around the jet axis) is in the same as the swirl direction, These results are in agreement with the conclusions of Liang and Maxworthy (2005).

The iso-surfaces of constant positive and negative helicity $H = (\boldsymbol{\omega}\mathbf{u})$ are shown in Figure 8a to demonstrate

the spiralling vortex structures in the low-swirl jet. Blue solid surface corresponds to negative H, whereas red semi-transparent surfaces visualize regions with positive H, including the jet vortex core. Eddies with helicity opposite to the jet core appear in the mixing layer, and their core lines are arranged along direction of the local velocity. Thus, the outer mixing layer of the low-swirl jet contains vortex filaments with positive and negative helicity, and both types of them are winded in the same sense as the jet swirl direction.

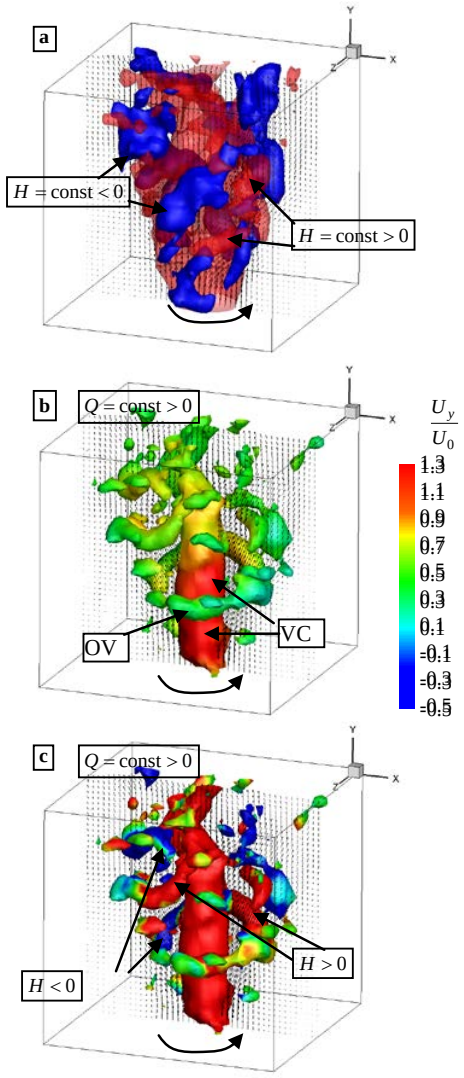

Fig. 8. The instantaneous velocity and vortical structures for a low-swirl jet (S = 0.41, Re = 8 900, 3D PIV). (a) - Positive (red) and negative (blue) helicity iso-surfaces; (b) and (c) - Q criterion colored by the axial velocity and helicity, respectively.

Figures 8b and c show iso-surfaces of a constant positive Q-criterion to visualise large-scale vortex structures. The colours of the surfaces in Figure 8b, indicating the local value of the axial velocity, show again that this velocity component is decreasing along the vortex core (VC). When the axial velocity reaches approximately half of the nozzle-exit value, the VC takes shape of spiral, which undergoes a spiralling breakdown. Near the nozzle (approximately one d) one can observe that the outer vortex structure (OV) is a curved ring vortex. During the vortex deformation the axial vorticity component is produced, and the helicity takes the opposite sign for different segments of the ring (see Figure 8c). Further downstream, the deformed ring breaks-up, resulting in longitudinal vortices with opposite sign of helicity.

To reveal the most energetic coherent modes in the velocity fields, a snapshot POD method (Syrovich, 1987) was applies to the measured sets of the instantaneous 3D velocity fields. The POD approach is based on the representation of each i-th instantaneous velocity field $\mathbf{u}_i$ as a finite series of products of spatial orthonormal basis functions $\boldsymbol{\varphi}_n$ with "time-dependent" coefficients a^i_n:

$$\mathbf{u}_i(\mathbf{x}) = \sum_{n=0}^{N} a_n^i \boldsymbol{\varphi}_n(\mathbf{x}), \text{ where } \left\langle \boldsymbol{\varphi}_i \boldsymbol{\varphi}_j \right\rangle_\Omega = \delta_{ij} \qquad (2)$$

Here, $\langle\,\rangle_\Omega$ denotes spatial averaging over a 3D domain, and δ_{ij} is the Kronecker delta. Following the snapshot method by Sirovich (1987), the basis functions $\boldsymbol{\varphi}_n$ can be represented as the following sum:

$$\boldsymbol{\varphi}_n(\mathbf{x}) = \sum_{k=0}^{N} A_k^n \mathbf{u}_k(\mathbf{x}) \qquad (3)$$

A variational problem for the optimal orthonormal basis (2) can be solved as a solution of a Fredholm integral equation of the second type, where the kernel of the integral operator is a cross-correlation function between the instantaneous velocity fields:

$$\frac{1}{N}\sum_{m=1}^{N} \left\langle \mathbf{u}_n(\mathbf{x})\mathbf{u}_m(\mathbf{x}) \right\rangle_\Omega A_m^i = \lambda_i A_n^i \qquad (4)$$

The solution to the eigenvector/eigenvalue problem (4) allows for the determination of N eigenvectors $\mathbf{A}^i = \{A_1{}^i \ldots A_N{}^i\}$ and corresponding eigenvalues λ_i for calculating the POD basis functions $\boldsymbol{\varphi}_n$. By virtue of the matrix symmetry, the eigenvalues have the following property: $\lambda_i > 0$ (for any i). Additionally, it is possible to apply the following condition: $\lambda_{i-1} \geq \lambda_i \geq 0$ (i = 1, …, N). The zero POD mode $\boldsymbol{\varphi}_0$ corresponded to the mean velocity field $\mathbf{U}$, and λ_i was related to spatially averaged values of the squared velocity fluctuations for the given mode.

In the present work, the problem (4) was solved, considering the matrix symmetry, using a QR algorithm to reduce the correlation matrix. In principle, the POD correlation matrix is not necessarily limited to the velocity data. POD can be applied, for example, for enstrophy, Lamb vector (Violato and Scarano, 2013) data.

Figures 9 and 10 show POD spectra for the high- and low-swirl jets of the decompositions of the velocity vector fields $\mathbf{u}$, helicity H, and Lamb vector fields $\mathbf{L} = [\boldsymbol{\omega}\times\mathbf{u}]$.

For the low-swirl flow the spectra show monotonous decrease of λ_i for all three types of POD inner product, where all spectra for the high-swirl jet are associated with two most energetic POD modes.

As Figure 11 shows, the amplitudes of the first two POD modes (associated with approximately 22% of TKE) of velocity in the high-swirl jet are scattered around a circle Lissajous figure.

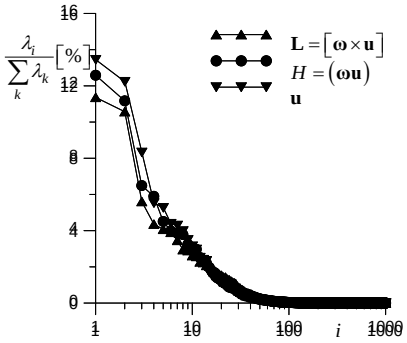

Figure 9. POD spectra of the instantaneous snapshots of velocity, helicity, and Lamb vectors for a high-swirl jet (S = 1.0 Re = 8 900, 3D PIV)

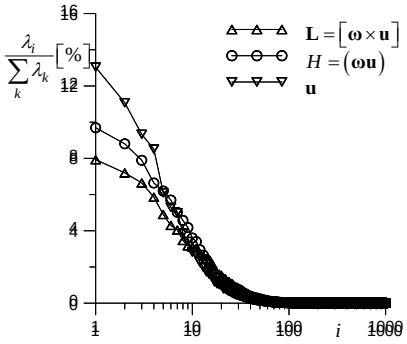

Figure 10. POD spectra of the instantaneous snapshots of velocity, helicity, and Lamb vectors for a low-swirl jet (S = 0.41 Re = 8 900, 3D PIV)

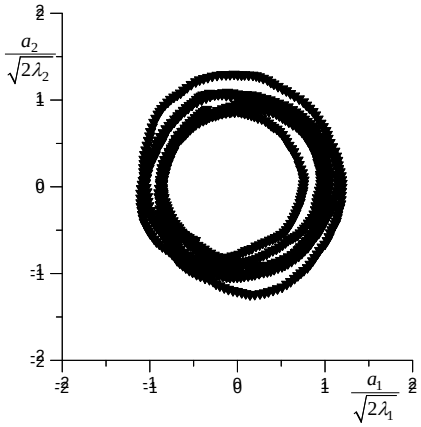

Figure 11. Correlation coefficients of first two POD modes of velocity fields for a high-swirl jet (S = 1.0 Re = 8 900, 3D PIV)

It is noted that the POD modes represent the same coherent structure, observed at different azimuthal angles (shifted by $\pi/4$). According to the low-order reconstruction, Eq (5) on the basis of the mean velocity field and the most energetic POD mode, the coherent structure represents a vortex structure around the jet axis and the outer helical vortex. The Q-criterion for the reconstruction is shown in Figure 12. The iso-surfaces are coloured according to the sign of the local helicity.

$$\mathbf{u}^{L.O.}(\mathbf{x}) = \boldsymbol{\varphi}_0(\mathbf{x}) + a_1^i \boldsymbol{\varphi}_1(\mathbf{x}) \tag{5}$$

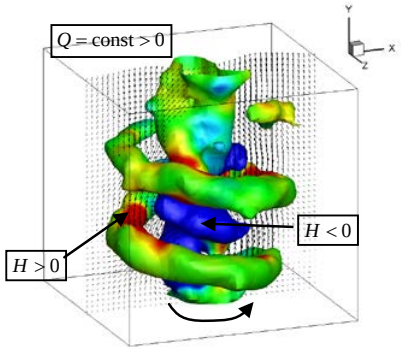

Figure 12. The instantaneous velocity data for a high-swirl jet (S = 1.0, Re = 8 900, 3D PIV)

The large-scale vortex structure around the jet axis is the vortex core of the jet, which transforms into a spiral around the region of reverse flow (region of negative helicity, shown by the arrow). The outer coherent structure is a helical vortex, and the sense of winding for this spiral is opposite to the sense of the mean swirl of the jet.

Similar 3D reconstructions were obtained previously from the 1D LDV (Cala et al., 2006) and 2D PIV measurements (Oberleithner et al., 2011; Alekseenko et al., 2012) in swirling jets with vortex breakdown. In the present study, the winding and rotation directions of the outer spiral are determined without assumptions and supports hypothesis behind the reconstruction of 2D PIV by Alekseenko et al. (2012).

Since the instantaneous 3D velocity fields were measured in the present work, the helical modes can be analyzed directly (without phase-averaging). This is done via a discrete Fourier transform with respect to azimuthal angle θ. Thus, each snapshot $\mathbf{u}$ (r, θ, y) is decomposed into the complex Fourier amplitudes $\hat{\mathbf{u}}$ (r, m, y), according to:

$$\hat{\mathbf{u}}(r,m,y) = \frac{1}{N_\theta}\sum_{k=1}^{N_\theta}\mathbf{u}(r,\theta_k,y)e^{-im\theta_k} \approx \approx \frac{1}{2\pi}\int_0^{2\pi}\mathbf{u}(r,\theta,y)e^{-im\theta}d\theta \tag{5}$$

This procedure requires data interpolation from the Cartesian coordinate system to the cylindrical mesh. This is done with a constant grid step in each direction, where. r is the radial coordinate defined as $r^2 = x^2 + z^2$. The

obtained squared values of the modes' amplitudes for different *m* are shown in Figures 13 and 14.

CONCLUSIONS

Types of vortex structures in turbulent low- and high-swirl (swirl rates S = 0.41 and S = 1.0) jet flows have been studied by POD of time-resolved tomographic PIV data. For the low swirl, vortex structures appeared in the form of tilted and deformed ring vortices around the jet vortex core. Downstream, the core takes shape of a spiral, and the rings evolved into helical eddies. The high-swirl flow was dominated by a pair of most energetic spiraling coherent structures: vortex core and the outer helical vortex

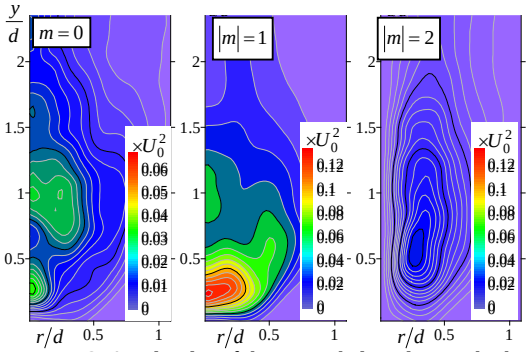

Figure 13. Amplitudes of the azimuthal modes in a high-swirl jet (S = 1.0 Re = 8 900, 3D PIV)

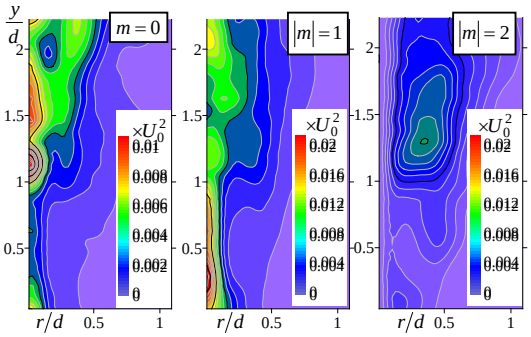

Figure 14. Amplitudes of the azimuthal modes in a low-swirl jet (S = 0.41 Re = 8 900, 3D PIV)

According to the analysis of the azimuthal modes, the mode |m| = 1 contained sufficient part of kinetic energy (more than two times greater than the modes |m| = 2) for both types flows. Consequently, it is concluded that the precessing vortex core phenomenon occurs in both low- and high-swirl jets. The vortex core was not extracted by POD in the low-swirl case because it was less energetic (according to the energy in mode |m| = 1) in comparison to the high swirl jet.

ACKNOWLEDGEMENTS

This work is funded by a grant from the Russian Science Foundation (No. 14-29-00203 in NSU, supervised by Kemal Hanjalic). Sergey Abdurakipov and Leonid Kozinkin are kindly acknowledged for data processing and useful suggestions.

REFERENCES

Alekseenko, M.V., Bilsky, A.V., Dulin, V.M., Kozinkin, L.A., Markovich, D.M., and Tokarev, M.P., 2014. Diagnostics of jet flows by using tomographic particle image velocimetry *Optoelectronics, Instrumentation and Data Processing*, Vol. 50, pp. 457-465.

Alekseenko, S.V., Dulin, V.M., Kozorezov, Y.S., and Markovich, D.M., 2008 Effect of axisymmetric forcing on the structure of a swirling turbulent jet. *International Journal of Heat and Fluid Flow*, Vol. 29, pp. 1699–1715.

Alekseenko, S.V., Dulin, V.M., Kozorezov, Y.S., and Markovich, D.M., 2012. Effect of high-amplitude forcing on turbulent combustion intensity and vortex core precession in a strongly swirling lifted propane/air flame *Combustion Science and Technology*, Vol. 184, pp. 1862-1890.

Atkinson, C.H. and Soria, J. 2009. An efficient simultaneous reconstruction technique for tomographic particle image velocimetry. *Experiments in Fluids*, Vol. 47, pp. 553–568.

Brücker, C., 1993. Study of vortex breakdown by particle tracking velocimetry (PTV), Part 2: Spiral-type vortex breakdown. *Experiments in Fluids*, Vol. 14, pp. 133–139.

Cala, C.E., Fernandes, E.C., Heitor, M.V., and Shtork, S.I., 2006. Coherent structures in unsteady swirling jet flow. *Experiments in Fluids*, Vol. 40, pp. 267-276.

Gupta, A.K., Lilley, D.G., and Syred, N., 1984 *Swirl flows.* Abacus Press, Kent Engl.

Hunt, J.C.R., Wraya A.A., and Moin ,P. 1988. Eddies, stream, and convergence zones in turbulent flows. *Center for Turbulence Research Report*, CTR-S88, p. 193

Johnson, M.R., Littlejohn, D., Nazeer, W.A., Smith, K.O., and Cheng, R.K., 2005 A comparison of the flowfields and emissions of high-swirl injectors and low-swirl injectors for lean premixed gas turbines. *Proceedings of the Combustion Institute*, Vol. 30, pp. 2867–2874.

Liang, H., and Maxworthy, T., 2005 An experimental investigation of swirling jets. *Journal of Fluid Mechanics*, Vol. 525, pp. 115-159

Markovich, D.M., Abdurakipov, S.S., Chikishev, L.M., Dulin, V.M., and Hanjalic, K., 2014. Comparative analysis of low- and high-swirl confined flames and jets by proper orthogonal and dynamic mode decompositions. *Physics of Fluids*, Vol. 26, 065109

Novara, M., Batenburg, J.K., and Scarano, F., 2010. Motion tracking-enhanced MART for tomographic PIV. *Measurement Science and Technology*, Vol. 21, 035401.

Oberleithner, K., Sieber, M., Nayeri, C.N., Paschereit, C.O., Petz, C., Hege, H.-C., Noack, B.R., and Wygnanski, I., 2011. Three-dimensional coherent structures in a swirling jet undergoing vortex breakdown: stability analysis and empirical mode construction. *Journal of Fluid Mechanics*, Vol. 679, pp. 383-414.

Sirovich, L., 1987. Turbulence and the dynamics of coherent structures Part I: Coherent structures *Quarterly of Applied Mathematics, XLV*, pp. 561-571

Violato, D., and Scarano, F., 2013. Three-dimensional vortex analysis and aeroacoustic source characterization of jet core breakdown. *Physics of Fluids*, Vol. 25, 015112

Wieneke, B., 2008. Volume self-calibration for 3D particle image velocimetry. *Experiments in Fluids*, Vol. 45, pp. 549-456.